

Developing Rapid Quenching Electronics for Coupling an Ion Trap to a Mass Spectrometer

Julia Katarina Pfatteicher

Advisor: Professor David A. Hanneke
May 7, 2019

Submitted to the
Department of Physics & Astronomy of Amherst College
in partial fulfilment of the
requirements for the degree of
Bachelors of Arts with honors

© 2019 Julia Katarina Pfatteicher

Abstract

The Standard Model is a profound collection of knowledge in the realm of physics which aims to define and explain the building blocks of matter. Amidst the clarity and power that the Standard Model grants, there are still remaining ambiguities about the fundamental particles that make up our existence. These ambiguities revolve around the elusiveness of dark matter and gravity. Leading theories predict the time-variations of fundamental constants as a key location where light may be shed and answers may be found to uncover the nature of these fundamental particles.

Molecules have been realized as a potential hotbed of information, as their sensitivities to nuclear motion may be exploited to reveal how with time, fundamental constants such as the electron-to-proton mass ratio (μ) can be altered to some precision. Using a radiofrequency ion trap as the residence for molecular ions and the sympathetically cooling atomic ions, a Coulomb crystal can form. Through resonance-enhanced multi-photon ionization (REMPI), state-selected O_2^+ ions are created. Then the vibrational transition is probed. Photons may drive the following dissociation, priming the particles for detection on a time-of-flight mass spectrometer (TOFMS). There the particles' masses may be precisely measured to determine if the vibrational transition was effectively driven. With this data we may learn more about the time variations in the electron-to-proton mass ratio.

In this thesis I describe the design of the electronics which will couple the ion trap to the TOFMS. This description includes background into the ultimate mission and theory of relevant concepts. In addition, the design process in practice will be outlined in detail, and further information on future ambitions will be delineated. The design centers around three main portions of the circuit. First is the tank circuit, which drives the trapping radiofrequency (RF) signal to the electrodes of the trap. Second is the quench circuit, which actively quenches, or stops, the RF signal. Third is the extraction voltage (EV) circuit, which drives high voltages to the electrodes for dispensing the ions out of the trap and towards the TOFMS. I demonstrate the use of the electronics by trapping ions and effectively switching from the radiofrequency voltage to the high voltage. I lay the path for future work to attach the TOFMS to the ion trap vacuum chamber and achieve successful extraction and detection of the ions. With this technology we aim to obtain measurements which may answer some of the compelling questions around the Standard Model, and illuminate new physics.

Acknowledgments

I am obliged to firstly thank my forever patient, attentive, and thorough thesis advisor, Professor Hanneke. For four years he has helped me gain my confidence in physics and push the limits of my abilities to places I could not have imagined I could go. It has been his ever-present faith in me which has allowed to me to even consider taking on an endeavor such as this. For his abundant faith in my success as well as his tedious ability to see it through, I am wholly grateful.

Thank you to Jim Kubasek for your consistent support and timeliness throughout my project. Thank you to Brian Creapeau for your support as well; your expertise has been tremendously helpful. The final execution of my work would have been impossible without you both.

To thank my mother feels like a colossal understatement. Without her enduring love, patience, and motivation (not to mention countless very long phone calls), none of my accomplishments would ever have even crossed my mind in the realm of possibilities. In everything I do, my success is hers too. Thanks, mom, for everything.

Thank you to my dad, Natasha, Stepan, and little Serafima for being such lights in my life and always making me laugh, even 500-some miles away. I am eternally grateful for your endless love, faith, and support.

And of course, thank you to all the friends, within and outside the department, for all you have taught me in the past four years. My experience at Amherst would have been unimaginably empty without you.

This material is based upon work supported by the Amherst College Dean of

the Faculty and by the National Science Foundation under grants PHY-125517 (CA-REER) and PHY-1806223 (RUI).

Contents

1	Introduction	1
2	Coupling the Paul Trap to the Mass Spectrometer	7
2.1	The Paul Trap	7
2.2	Significance of the Mass Spectrometer	12
2.3	Theory of Electronics	15
3	Circuit Board Design and Construction	18
3.1	The Transformer	18
3.2	Switching Behavior	23
3.3	Circuit Design Considerations	28
4	Implementation and Ion Clouds	36
4.1	Connecting the Board to the Trap	36
4.2	Trapping Ions	40
4.3	Applying the Board to Test Switching	43
5	Concluding Thoughts	45
5.1	Small-Picture Goals	45
5.2	Big-Picture Goals	49

List of Figures

1.1	Coulomb Crystal	3
1.2	Ion Trajectories	4
2.1	Electrode Diagram	8
2.2	Solutions to Mathieu Equations	10
2.3	Lowest Stability Region of Mathieu Equations.	11
2.4	Dissociation Technique	13
2.5	TOFMS	14
2.6	Block Diagram	16
2.7	Trapping and Extracting Electrodes	17
3.1	Resonant Frequency Selection	21
3.2	Voltage Selection	22
3.3	Impedance Matching	22
3.4	MOSFET	24
3.5	Board Schematic	25
3.6	The Circuit Board Design	27
3.7	The Printed Circuit Board	28
3.8	Oscilloscope of Left Side of Board	29
3.9	Oscilloscope of Original Board	32
3.10	biMOSFET	33
3.11	Oscilloscope of Updated Signal	34
3.12	Quenching and Extracting Voltages	35
4.1	Circuit Board Attached to Ion Trap	38
4.2	First Image of Ions	40
4.3	Four Beryllium Ions with Two Dark Ions	41
4.4	Ions Forming Diamond	42
4.5	Micromotion of Ions	43
5.1	Structure of MOSFET and its Internal Capacitances	47

Chapter 1

Introduction

"Just before our love got lost you said,
'I am as constant as a northern star' and I said,
'Constantly in the darkness,
Where's that at?
If you want me I'll be in the bar'" - Joni Mitchell

“Definition” is both a provocative and a precarious term in its common usages within scientific fields. As comforting as it is to define something with certainty, often this certainty comes from either misunderstanding or dismissed nuances, which may shift or even null this definition. “Constant,” too, is a word in both colloquial and scientific realms that is often conflated with “constant enough, right here, right now.” We may wish to explore the terms under which it is not enough, and when space and time circumstantially alter these so-called “constants,” as even Joni Mitchell contemplated [1].

Within the physical sciences, one of the few things we are taught to trust with good faith are the fundamental constant values we often find in the backs of books. This may include the electron charge, \hbar , or the gravitational constant. Yet the more we learn about these constants, the more we may be compelled to question their nature and the process by which we have defined them with such certainty. The Standard Model aims to classify values pertaining to the elementary particles that

we so deeply wish to define, to understand, to categorize. Through the pursuit of my honors thesis I hope to contribute, in some small way, to a broader understanding of how these constants may vary through time, which may illuminate new physics and potentially improve our comprehension of dark matter and its properties.

Our research aims to discover more about these fundamental constants which make up the Standard Model, namely the time variation in the proton-to-electron mass ratio $\mu = m_p/m_e$. Molecules contain myriad internal degrees of freedom, making them ideal candidates for observations such as these, especially involving the degrees of freedom which pertain to nuclear motion where changes in μ are especially sensitive [2]. In particular, we drive vibrational transitions within molecules and observe the transition frequency over time. Time variations of the frequency will point to variations in μ as well, uncovering new phenomena [3].

In order to achieve these precise measurements relating to μ , we drive two-photon transitions between vibrational states. Calculated transition rates and systematic shifts assist our analysis [2]. Since O_2^+ is homonuclear, it is nonpolar. Because of this symmetry, for any electronic state, half of the rotational states are eliminated. Therefore, electric dipole transitions are forbidden between rotational and vibrational states within the same electronic state. Instead, we electric-dipole couple to other excited electronic states as a means of achieving two-photon transitions [4–7].

Photoionization is an ideal means of preparing the ions as it allows us to create state-selected ions. State preparation is not feasible with other strategies such as optical pumping, because O_2^+ is nonpolar [8]. Through resonance-enhanced multiphoton ionization (REMPI), we can drive the molecular transition to ionize oxygen molecules. Resonance-enhanced photoionization decreases the number of possible ionic states, as seen in aims for precise vibrational selectivity [9–13].

First the O_2^+ molecules are prepared in their vibrational ground state via photoionization, with 2+1 photons at 301 nm. Next the vibrational transition is driven

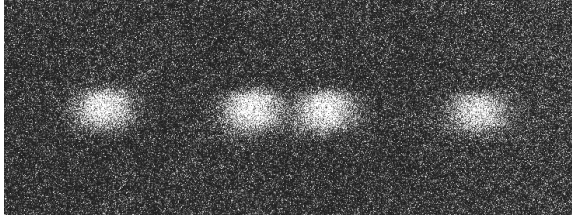


Figure 1.1: Image of four beryllium atomic ions and two molecular ions forming an ion cloud, or Coulomb crystal, inside the ion trap. Molecular ions occupy the dark space between fluorescing ions. The distance between the innermost bright ions is $25\ \mu\text{m}$, while the distance between the first and second bright ions is $51\ \mu\text{m}$.

by two photons, followed by one photon which dissociates the molecule. To detect the transition, we may drive state-selective dissociation and then detect the remaining ions through mass analysis. Only molecules which have reached this vibrational transition will be capable of dissociation.

A linear Paul trap is implemented to trap ions, allowing for extended probe times for driving these transitions. Molecular ions are then co-trapped with atomic ions (Be^+) inside the trap. The atomic ions act as a source of translational cooling as well as a means to detect presence and motion of molecular ions. An ultraviolet (UV) beam crystallizes and fluoresces the ions. The UV light will cause beryllium ions to fluoresce while the oxygen ions will not. A camera is implemented to witness the resultant ion cloud formation (see Fig. 1.1).

Our trap is a radiofrequency Paul trap, consisting of four main electrodes (some of which have multiple segments). By applying a radiofrequency (RF) voltage to the electrodes, the center of the trap is at a dynamic equilibrium. When multiple ions are held within the trap's confining electric fields, the ions assemble into a centered cluster.

We call the cluster of ions at the center of the trap a Coulomb crystal (Fig. 1.1) because the ion motion is controlled via Coulomb repulsion and the ions align in a lattice formation. This equilibrium is both dynamic and stable, creating consistent

particle motion in three dimensions.

The motion in each dimension is oscillatory. When the x and y directions of motion are related by a factor of 2, the motion outlines a hyperboloid-like shape. The 2D projection of this motion is shown in Fig. 1.2. The ions' trajectories are described by both the secular frequency, which drives the hyperboloid-like motion, and the high frequency micromotion.

In the axial, or z direction, there is only one frequency of oscillation. Fig. 1.2 shows ion trajectories of a typical Paul Trap (x and y in our case), though the trapping parameters of our ions are different as well as the geometry of our trap. Therefore the figure should be considered a helpful conceptual guide, not a thorough demonstration of the lab's achievements.

This potential field is capable of probing the ions for long periods of time to

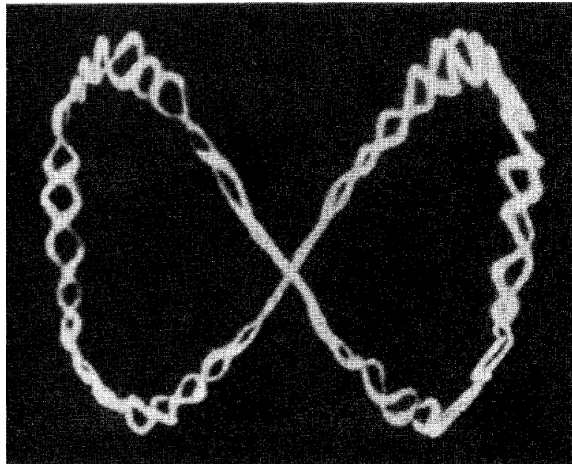


Figure 1.2: 2D projection of 3D motion of the ion trajectories in a Paul Trap. The secular frequency describes the overall hyperboloid motion, seen as a figure 8-like shape in 2D here. The additional high frequency motion is the micromotion. Ion trajectories are depicted for a hyperbolic trap, specifically. Figure from [14]; used with permission.

allow for precise measurements. In order to measure the success of the transition precisely, an outside form of detection is needed. Others implement strategies such as resonance-enhanced threshold-photoionization followed by laser-induced charge trans-

fer to probe the crystal’s composition [15, 16]. Some use blackbody radiation or optical and resonance-enhanced photon dissociation as a means for detection for polar molecules [8, 17]. Broadband rotational optical cooling is alternatively used with heteronuclear molecules to drive to the ground rotational state [18].

In our setup we implement a time-of-flight mass spectrometer (TOFMS), capable of detecting particle time of arrival on the detector. We first eject the particles cleanly out of the vacuum, so as not to disturb the formation and makeup of the ion cloud. Then they need to be accelerated with an electric field before being subject to detection. Next, a mass spectrometer fulfills the purpose of detecting the particles within the ion cloud to a high precision. By detecting the particles’ time of arrival, their speeds can be determined. Since all particles have the same charge, they will also have the same energy, therefore their mass can be determined simply by comparing the electric energy with the kinetic energy:

$$qV = \frac{1}{2}mv^2 \tag{1.1}$$

With the known mass of each particle, the identities of the particles and their abundance can be determined.

This knowledge and previous experimentation leaves us with the upcoming goal of uniting these two systems, the ion trap and the TOFMS. My project focuses on coupling the ion trap to the mass spectrometer so that we may conduct this experiment successfully and obtain fruitful data to uncover insight on the complexities of the physical world. The goal of the electronics is to provide both trapping and extracting potentials on the ion trap’s electrodes, and to allow for fast switching between the two. This functionality enables us to trap and manipulate the particles until we are ready to dump them to our detection mechanism. To do so requires the rapid quenching the trapping potential, which is the active removal of the RF signal, to allow for

short dissipation times (less than 2 RF cycles [19]). We then apply the high DC extraction voltages to expel the ions cleanly out of the trap. The electronics consist of three main parts: The tank circuit, the quench circuit, and the extraction voltage (EV) circuit. The tank circuit drives the RF signal to the electrodes to provide the trapping functionality. The quench circuit actively removes the RF signal to prepare for extraction. The EV circuit applies high extraction voltages to the electrodes for cleanly expelling all ions out of the trap.

In the following pages I create the framework of the theory, process, and practice of this experiment in its entirety and expand upon its relevance, context, and potential future usage. We will begin with the theory relating to the experimental setup as well as the electronics for coupling the trap to the mass spectrometer (Chapter 2). This section will additionally explain in detail the operation of the Paul Trap and the mass spectrometer themselves. Then we will transition into a thorough description of the circuit design, setup, and construction (Chapter 3). Here I will describe the methods and strategies used for circuit development. Next we will examine the application of the circuit and its capabilities and limitations (Chapter 4). Finally we will conclude with closing thoughts and future ambitions (Chapter 5).

Chapter 2

Coupling the Paul Trap to the Mass Spectrometer

In this chapter I will discuss the theoretical background needed to understand the experimental setup and lab's goals. This will include a discussion of the Paul Trap, which acts as the central component of the lab, as well as the TOFMS, which is our outside form of detection. This section will also discuss the theory of the electronics needed to couple these two elements, detailing how the trap's electrodes may both trap and expel ions.

2.1 The Paul Trap

Trapping ions requires precise control of charged particle movement within a narrow stability region where ions can achieve stable equilibrium. Our charged particle trap is called a Paul Trap, coined for Wolfgang Paul's groundbreaking research in 1953 around trapping charged particles with an electric field [20]. In our case, four electrodes run parallel to one another to form the trap. Two rods diagonal from each other act as our "RF electrodes," or the trapping electrodes whose potential oscillates at radiofrequency. These rods trap ions radially. The other rods, also diagonal from

one another, have a DC voltage across them at AC ground. They are segmented into five parts to allow for axial trapping (see Fig. 2.1). As mentioned in Chapter 1, the

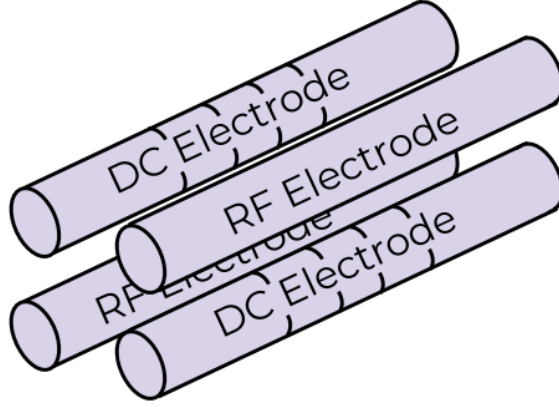


Figure 2.1: Diagram of the electrodes in trapping mode. The DC electrodes are segmented to control axial trapping, while the RF electrodes control radial trapping.

electrodes create a dynamic stable equilibrium at the center of the trap. This can be understood by considering the electric potential for an RF trap. We first may observe that the the general potential can be broken down into two time-dependent parts: one of which is static while the other varies sinusoidally at the RF frequency Ω [21]:

$$\Phi(x, y, z, t) = U \frac{1}{2}(\alpha x^2 + \beta y^2 + \gamma z^2) + V \cos(\Omega t) \frac{1}{2}(\alpha' x^2 + \beta' y^2 + \gamma' z^2) \quad (2.1)$$

where U represents the DC voltage and V represents the radiofrequency signal's maximum voltage amplitude. We also know that the potential must satisfy Laplace's equation, $\nabla^2 \Phi = 0$, at any point in time. This further restricts the parameterization of the potential, leading to:

$$\alpha + \beta + \gamma = 0 \quad (2.2)$$

and

$$\alpha' + \beta' + \gamma' = 0 \quad (2.3)$$

With these limitations we can see that there is no way to create a local static equilibrium ($V = 0$), so the solution must be dynamic [21]. In our case, we implement a linear trap which creates a static confinement in the z direction and a dynamical confinement in the x - y plane. Therefore, the confinement looks like:

$$-(\alpha + \beta) = \gamma > 0 \quad (2.4)$$

and

$$\alpha' = -\beta' \quad (2.5)$$

$$\gamma' = 0 \quad (2.6)$$

With a classical approach, the primary equation of motion is:

$$\ddot{x} + \frac{e}{mr_o^2}[U - V \cos(\Omega t)]x = 0 \quad (2.7)$$

where e is the ion charge, m is the electron mass, and r_o is a characteristic length scale of the trap that is on the order of the distance from the ions to the electrodes. r_o relates to α' such that

$$\alpha' = \frac{1}{r_o^2} \quad (2.8)$$

Eq. 2.7 is given for the x direction, though the radial confinement in y is of the same form. The coefficients differ, though, since our trap is deliberately asymmetrical, as the two radial trap frequencies are not the same. This is because we apply the DC potentials only to one pair of the electrodes while the RF electrodes are at DC ground (see Fig. 2.1). If we let

$$a = -\frac{4eU}{mr_o^2\Omega^2}; \quad q = \frac{2eV}{mr_o^2\Omega^2}; \quad \zeta = \frac{\Omega t}{2} \quad (2.9)$$

then we have the Mathieu differential equation [20] [21]:

$$\frac{d^2x}{d\zeta^2} + [a - 2q \cos(2\zeta)]x = 0 \quad (2.10)$$

The solutions to the Mathieu differential equations are divided into two classes: those with stable trajectories and unstable trajectories. With a nonlinear second order differential equation such as this, certain mathematical strategies may be employed [22]. The solution is an exponential, with a periodic coefficient. If the exponent takes on an imaginary number, the function will exhibit oscillatory behavior and remain bounded, creating a stable solution. If the exponent takes on a real number, positive or negative, then the solution will be unbounded as it approaches positive or negative infinity, respectively.

The pairs of a and q parameters can be plotted in a map, where one can see the space in which the particles may reach stable equilibrium [23].

Fig. 2.2 visually depicts where the ions may be trapped in a stable equilibrium,

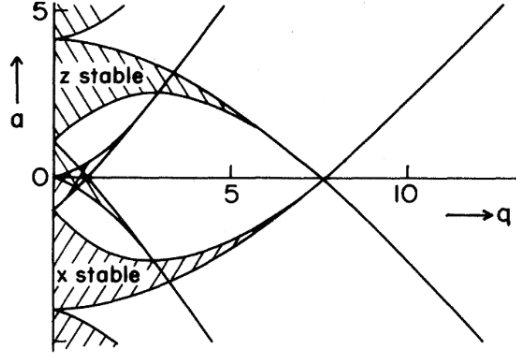


Figure 2.2: Graph of the stability regions of the Mathieu equations. Figure is given for the z and x directions, while our configuration lends the same graph in x and y . Figure from [14]; used with permission.

which we are seeking. Outside these regions of stability, the ions can be at equilibrium, but it will be unstable. Given that we want the ions to stay in the trap for

long periods of time, a stable equilibrium needs to be achieved. In particular, we are interested in the lowest stability region (see Fig. 2.3).

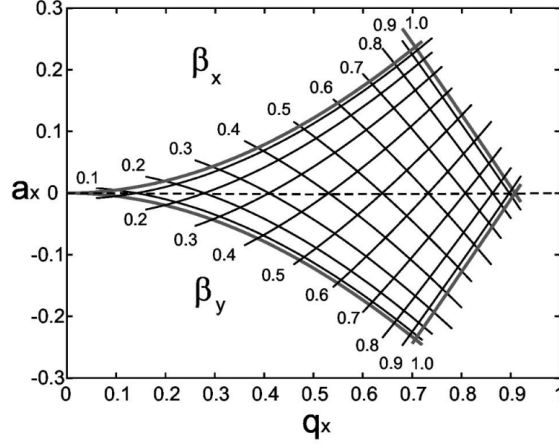


Figure 2.3: Zoomed in graph the lowest stability region of the Mathieu equations. Figure from [21]; used with permission.

By finding the common solution to these differential equations, and manipulating the equations a bit, we can conclude that the fundamental motion of the charged particles oscillates at a frequency of

$$\omega_0 = \frac{\beta\Omega}{2} \quad (2.11)$$

where β describes the limits of stability in two dimensions and can take on values from 0 to 1. We assume that the frequency of the micromotion and the secular frequency are different enough such that a and q^2 are much less than 1. Otherwise the trajectory may be stable but it will not be well described by a secular frequency plus micromotion. If the value exceeds 1, the ions' motion away from the null would exceed the limits of confinement and the ions would leave the trap.

With that approximation in mind, we find that

$$\beta_x \approx \sqrt{a_x + q_x^2/2} \quad (2.12)$$

Which we may apply to Eq. 2.11 to solve for the trap frequency of a stable solution for the general radial motion r :

$$\omega_r = \frac{q\Omega}{2\sqrt{2}} \quad (2.13)$$

Given the equation above, we may find the precise frequency of the voltage needed to achieve the desired trap frequency that lies in the region of stability. A q value of about 0.3 would be favorable, because it would yield a q^2 value of less than 0.1. To maintain a strong enough trap, we are aiming for the q value to be no lower than this. Therefore ideal trap frequency is such that:

$$\frac{\omega_r}{2\pi} = 1 \text{ MHz} \quad (2.14)$$

We can then calculate that a practical voltage frequency value, $\frac{\Omega}{2\pi}$, should be about 9-10 MHz. These constraints yield a confinement that compromises between a higher trap frequency while keeping $q^2 \ll 1$.

2.2 Significance of the Mass Spectrometer

Once we have our ions trapped in stable equilibrium inside the trap, we can dissociate the molecular ions so as to detect if the transitions we aim to drive have been driven successfully. We first drive the vibrational transition with two photons, then dissociate them with another photon at a separate wavelength. Only the molecules whose transitions have been driven effectively will be able to achieve dissociation (see Fig. 2.4). In order to detect if dissociation has occurred, we utilize an outside form of detection. The TOFMS acts as a means of detecting the ions, implementing a

microchannel plate as the final destination for measuring the ions' speed [3].

The mass spectrometer itself is an essential piece of the puzzle for our experiment.

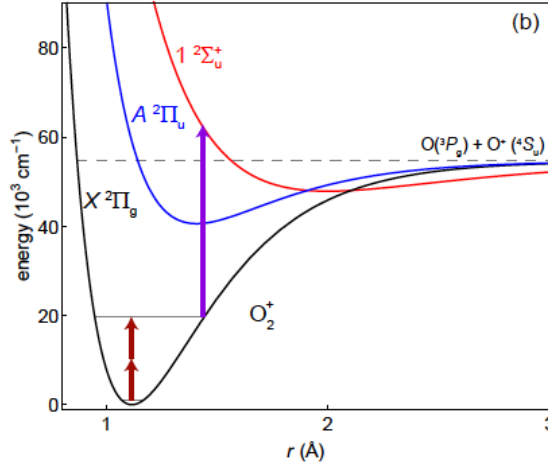


Figure 2.4: Diagram of the two photon transition, driving the vibrational overtone, and the last photon driving dissociation for molecules which have successfully reached the excited vibrational state. Figure from [2]; used under Creative Commons Attribution (CC BY) license.

Although the exciting (both literally and figuratively) events involving the particles happen inside the ion trap, our understanding of the trap's contents is tightly restricted without a detection mechanism.

Using basic electromagnetism and kinematics, the theory of the TOFMS can be understood. We begin with a charged particle of mass m and charge q . Two parallel electrodes with a voltage V between them create an electric field, and therefore a region of acceleration. After emerging from this region, the particles enter a zero-field region of a precise length l . This region is especially important because the particles can move freely with no forces acting on them. At the end of the zero-field region is the MCP, where the particles' time of arrival is measured (see Fig. 2.5). With our knowledge of the system, and some simple introductory physics equations, we can conclude that all the particles will emerge from the acceleration region with the same

energy, therefore:

$$qV = \frac{1}{2}mv^2 \quad (2.15)$$

We can then solve for the time of arrival:

$$t = \frac{l}{v} = l\sqrt{\frac{m}{2qV}} \quad (2.16)$$

Since we know the voltage V , the time of arrival is solely dependent on the mass-to-charge ratio. In our particular experiment, all the particles of interest have the same charge. Therefore, we can use the time of arrival to determine the ion's mass, and therefore its identity. The mass ratio between the undissociated O_2^+ , the dissociated O^+ , and Be^+ is 32:16:9, which will be indicated by the time of arrival ratio 5.7:4:3 on the MCP (due to the square root in Eq. 2.16). With this information we can determine the abundance of each ion and precisely determine their time of arrival. All other signals may be attributed to background gas.

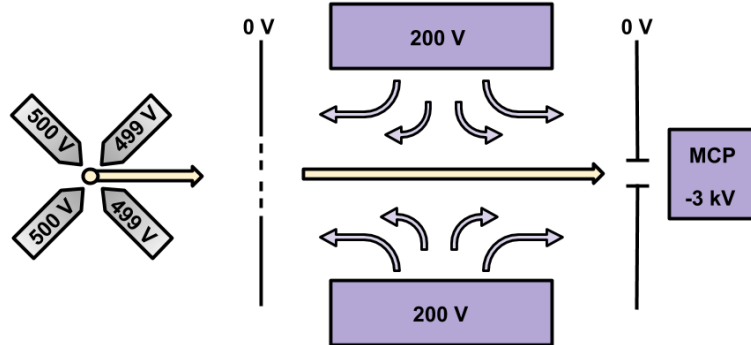


Figure 2.5: Block diagram of the extraction TOFMS process. The potential difference between the high voltage of the trap electrodes and the 0 V plate creates the acceleration region. The ions then pass through the grid electrode and enter the lens created by the 200 V plates, which bends the ions towards to middle to maintain the ions' trajectory towards the MCP. The focus of the lens is at the detector. From the lens the ions travel to the MCP for detection. All regions are under vacuum.

2.3 Theory of Electronics

To unite the mass spectrometer with the ion trap, it is first necessary to “untrap” the ions and then expel them towards the TOFMS. By switching the voltage application on the electrodes of the trap from the trapping function to the extracting function, the Coulomb crystal can be properly accelerated to the detector for analysis. To do so requires an electronic control of the voltages, which can switch rapidly, and therefore cleanly, from a radiofrequency AC voltage (about 200 V at a frequency of 10 MHz) to a high DC voltage (about 500 V). For proper functionality of the mass spectrometer, the trap must shut off within about 1-2 RF cycles so as not to compromise the resolution of the detector due to distortion from the extraction field [19]. If the RF signal is given time to dissipate, the q factor decreases, causing the ion cloud to expand which disturbs the form of the Coulomb crystal. By switching the RF off quickly, the ion cloud can maintain its shape as it is extracted. Furthermore, any small difference in distance between the trap and the detector between the ions in the front of the cloud and those in the back is accounted for: the ions in the back of the cloud will be subject to a stronger force from the back electrodes than those in the front, accelerating them forward more so that all the ions leave the trap at the same time.

The circuit is composed of three main parts. First is the tank circuit, which drives the function generator signal to the electrodes. Second is the quenching circuit, which powers the active removal of the RF. Third is the extraction voltage portion of the circuit, which drives the high extraction voltages to the electrodes (See Fig. 2.6).

We implement an RF switch, which is switched on to drive the signal from the function generator to the extraction circuitry. The switch connects to a transformer, capable of amplifying the voltage as well as setting the resonant frequency. The transformer is made of one primary coil and two secondary coils to ensure proper operation (see Chapter 3 for more). Then the signal is driven to two MOSFETs

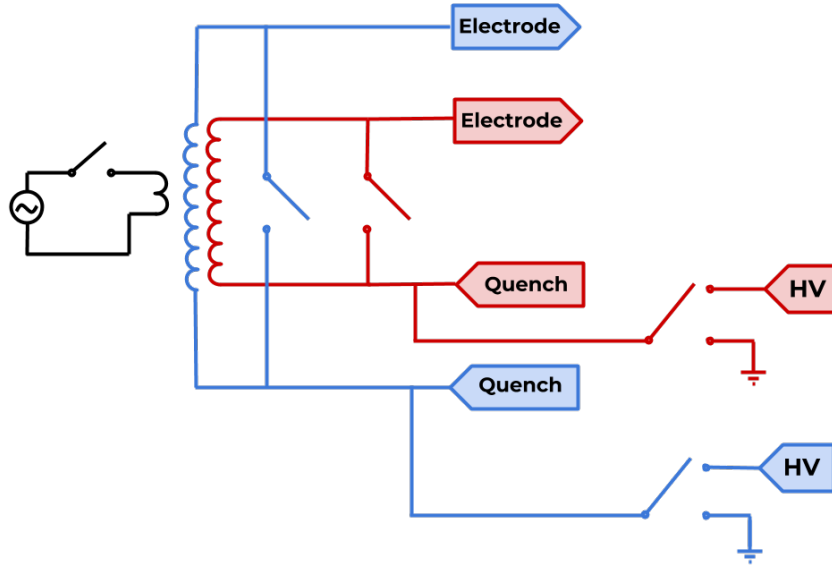


Figure 2.6: Block diagram of the circuit design. Blue indicates the first secondary winding and its circuit parts, while red indicates the second secondary. The RF section indicates the tank circuit, where we drive the RF signal. The quench section in the middle contains the switch which turns off the RF signal. The extraction section contains the switch which applies the high voltage signal for extraction.

(metal-oxide semiconductor field-effect transistors), which operate as power switches. These switches determine when the trapping voltages are being applied to the electrodes, and when the extraction voltages are applied.

Fig. 2.7 depicts the electrodes in both their trapping and extracting functionalities. The RF switch, as well as the MOSFETs, allow us to switch between both uses. Further explanation of the circuit design and operation is delineated in Chapter 3.

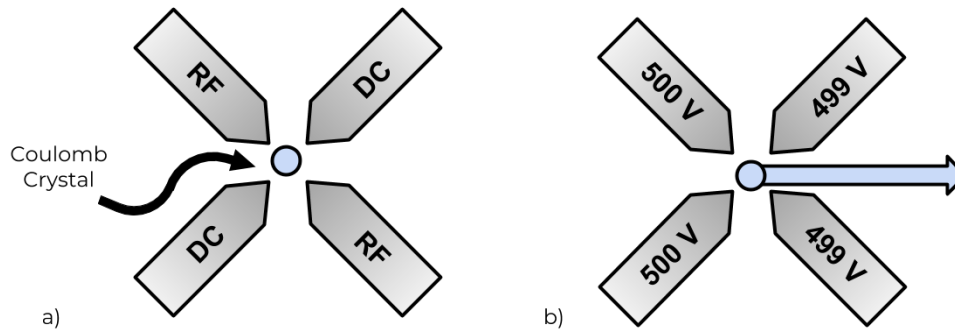


Figure 2.7: Diagram of the electrodes and their dual functionality. The voltages of each electrode are labeled for each phase. (a) The RF signal is applied to the trap's electrodes, implementing the trapping functionality. (b) The HV signal is applied to the electrodes, implementing the extraction functionality.

Chapter 3

Circuit Board Design and Construction

A robust description of the electronics' goals will be provided in this chapter. I will outline the steps taken to design and create the printed circuit board that will couple the ion trap to the TOFMS. First I will detail the significance and design of the transformer as the central RF component of the board. Then I will explain the switching operation of the board and thoroughly outline its electronic functionality.

3.1 The Transformer

The central component of the circuit design is the transformer. It acts as an amplifier for the RF signal and sets the resonant frequency of the trap, as the secondary winding forms a resonant LC circuit with the capacitive load of the trap. The LC circuit acts as a resonator, capable of storing energy. Since the trap behaves capacitively in this case, high voltage is needed rather than high power. A large step-up transformer allows for a substantial step up in voltage.

Considering this portion of the circuit as an LC resonator, we can set the circuit's

resonant frequency using

$$f = \frac{1}{2\pi\sqrt{LC}} \quad (3.1)$$

where f is given in units of Hz. So, we can set the resonant frequency given the capacitance of the trap (about 10 pF) by selecting the inductance of the transformer's secondary winding.

The secondary's inductance is set by a multitude of factors. We must first consider the inductance constant, A_L , of the transformer core. This value directly relates to the permeability of the core and determines the turns needed to achieve a certain inductance value. The inductance constant is an intrinsic property of the core and is set by its make and material. The general relationship between the inductance constant, the number of turns, and the inductance is [24, Section 4.60]:

$$L = A_L(N_{turns})^2 \quad (3.2)$$

If A_L is in nH/t² and L is in mH, then Eq. 3.2 becomes

$$N_{turns} = 1000\sqrt{\frac{L}{A_L}} \quad (3.3)$$

So, if we favor a step-up transformer with more turns on the secondary, then a lower inductance constant is needed for a certain inductance. We also favor a core with a larger diameter, to give space for a generous number of secondary turns. The core that most closely aligned with these preferences was a sendust toroidal core with an inductance constant of $A_L = 24$ nH/t² and a diameter of 36.7 mm¹. Other cores were tested and considered, but this one met our specifications best.

We also needed to optimize the windings using impedance matching to achieve the maximum output voltage. Impedance matching is the process of selecting the

¹77326A7, Magnetics, Inc.

optimal input impedance correlating to the output impedance so as to maximize the power transfer. To do so, the number of primary turns is varied until the maximum output voltage is reached.

With transformers, experimental testing is always necessary. Myriad factors, such as winding spacing, wire gauge, and core manufacturing variations may contribute to the outcome in practice that the theory cannot always predict. Experimentation included the controlled varying of these factors, in addition the the number of turns on the primary and secondary, to optimize the performance of the transformer. Optimization was characterized by achieving the maximum output voltage while maintaining a resonant frequency in the range of 10 MHz.

First we considered the winding spacing on the transformer. If the turns become close enough together, capacitive coupling between turns would create a mini-resonant circuit within the transformer. Then the transformer would have its own resonance which would need to be considered in selecting the resonant frequency of the actual resonant circuit. We experimented with the winding spacing to measure the effects of this possible capacitive coupling, but concluded that the effects were marginal and did not need to be accounted for in the construction of the transformer.

The wire gauge can impact the resistance of the wire, such that an increased gauge corresponds to a smaller wire and an increased resistance. Increasing the wire gauge up to 32, we found that such a thin wire was not creating reproducible data due to its flimsiness and high resistance. These factors allowed us to determine that such a high wire gauge was unsuitable. Wire gauges below 20 were thick enough that they were difficult to wrap around the transformer core, and inhibited our ability to increase the step-up ratio and therefore maximize output voltage. Ultimately a wire gauge of 24 was selected as an optimal solution.

Determining the ideal number of turns on both the primary and secondary required thorough measurements to conclude the relationship between the two. As aforemen-

tioned, impedance matching plays a key role in calculating the optimal ratio. Before considering impedance matching, though, the optimal secondary turn number needed to be determined, since that number alone sets the resonant frequency of the circuit. Ultimately the ideal number of turns on the secondary was determined to be 20 (as seen in Fig. 3.1 and Fig. 3.2). This allowed for a substantial voltage output while still achieving a sufficiently high resonant frequency (10 MHz, so as to achieve a 1MHz trap frequency). We ran the function generator with a 50Ω output impedance at 4.00 V peak-to-peak with 0 V offset. In this testing phase we used the scope probes as our source of capacitance, running at 10X attenuation, correlating to 10 pF (a fair approximation to the trap capacitance).

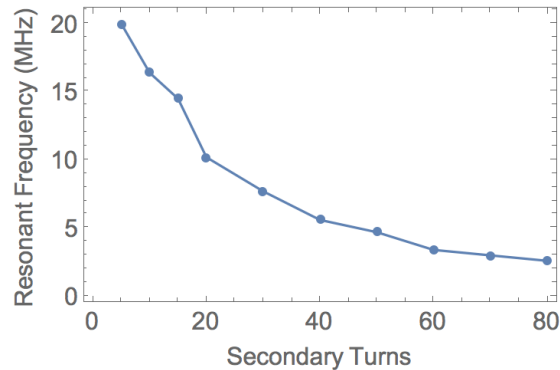


Figure 3.1: Optimization of secondary windings with resonant frequency. At 20 turns, frequency reaches 10 MHz. Data taken with 5 turns on the primary.

Once the secondary number of windings was set to lock in the inductance value, the primary number of turns needed to be set to optimize the output voltage. Naively, it would seem that the lower the number of turns on the primary, the higher the step up, so the higher the output voltage. In practice, though, this is not the case for our scenario. Since we are dealing with a higher frequency signal than those of conventional transformers, the impedance of the secondary and primary feed back into one another, affecting the output voltage. To locate the optimal number of turns

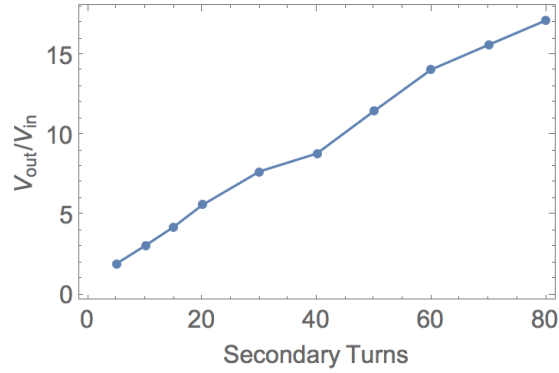


Figure 3.2: Relationship between secondary windings and voltage. Voltage is given as a ratio of output voltage to input voltage. At 20 turns, the voltage ratio is 5:1. Data taken with 5 turns on the primary.

on the primary, it was necessary to account for this via a process called impedance matching. As seen in Fig. 3.3, 4 turns on the primary optimize the output of the transformer when set to 20 turns.

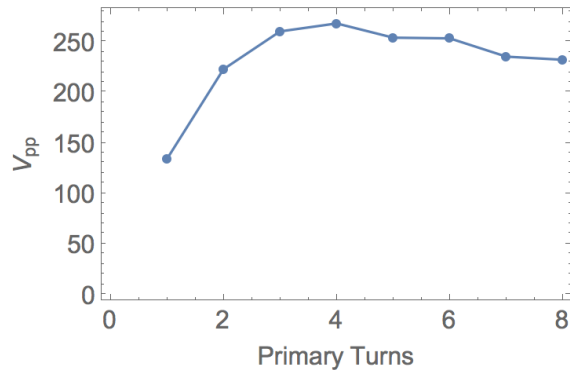


Figure 3.3: Optimization of primary turns using impedance matching. Voltage input is $4 V_{pp}$. Voltage output peaks at 4 turns.

In addition to calculating the optimal winding ratio, the optimal power input needed to be determined. Although we are not looking to maximize power, but rather voltage, it is still important to locate an ideal power input. Varying the power in terms of dBm, the transformer began to heat up at about 30 dBm, or 1 W. Once it reached 36 dBm, or almost 4 W, it was considerably hot. Heating of the transformer

should be avoided, or else an outside cooling system would become necessary. It was eventually determined that 28 dBm (about 0.6 W) would be an optimal and safe amount of power to put into the transformer.

3.2 Switching Behavior

Zooming out to the overall circuit design, the switching functionality of the circuit is paramount. As mentioned in Section 2.3, the MOSFETs control this vital switching behavior. Since our transistors act as power switches, they turn on or off the power to a load (in our case the electrodes).

The anatomy of the MOSFET can be visualized in Fig. 3.4. They are enhancement n-channel MOSFETs, meaning that they are off at zero gate-source voltage, and to turn them on the gate voltage must be pulled higher than the source voltage. When the transistors on the quench circuit are closed, the transistors form a low-resistance current path as the source and drain are shorted to each other, shorting RF signal across the secondaries to ground and actively stopping it. When open, the RF can flow freely from the secondaries to the electrodes for the trapping functionality, as the source and drain are isolated (see Fig. 3.4).

There is one MOSFET for each secondary, as there is one quench circuit for each. In the extraction voltage portion of the circuit, multiple MOSFETs are also used. Two transistors are used for each secondary's extraction voltage (EV) portion, creating a push-pull configuration, as one transistor operates the low voltage side and the other the high voltage side. The low voltage side MOSFET's gate is driven by a driver chip, and the high voltage MOSFET's gate is driven by a driver chip with an optocoupler. Both sides are powered by a DC/DC converter. In the trapping stage, the high voltage MOSFET is kept open, therefore not connected. The low voltage

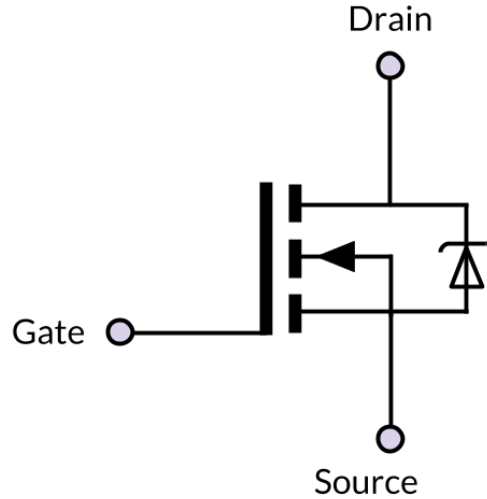


Figure 3.4: Diagram of an enhancement n-channel MOSFET.

MOSFET is closed, creating a ground connection for one side of the secondaries while the other carries the RF to the electrodes. In the extraction stage, the high voltage MOSFET is open while the low voltage MOSFET is closed, activating the extraction voltage circuit to apply the HV signal for extraction. As aforementioned, this portion of the circuit is doubled so as to apply two different extraction voltages for the electrodes of either side of the trap (see Fig. 2.7 b). The quench circuit consists of similar components, with a MOSFET driven by the driver chip connected to an optocoupler, powered by a DC/DC converter.

Since the MOSFET can handle large drain-to-source voltage but not a large gate-to-source voltage, all the gate electronics needed to be able to float to the high voltage. For this reason we implement the DC/DC converter, which allows the circuit to float while maintaining the 12 V which powers the rest of the components. Since switching the gate quickly requires a lot of current, the driver chip is implemented to provide sufficient current. An inverted driver chip is used, as the optocoupler inverts the signal. For the low voltage side of the extraction portion of the circuit, an inverted driver chip is used as well, since we want it to be inverted from the HV side, turning

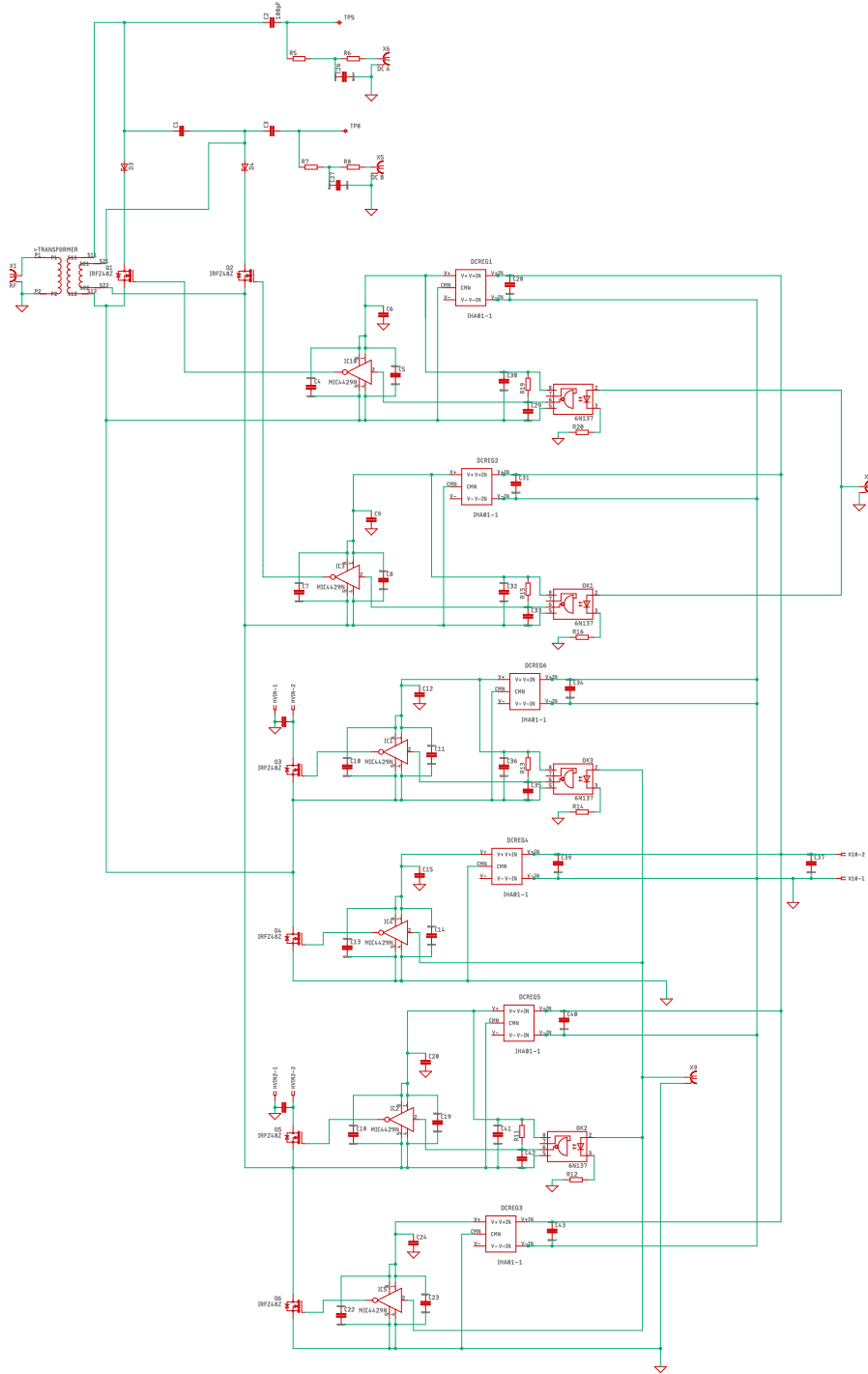


Figure 3.5: Unabbreviated schematic of the board design.

it off when the HV is on and vice versa.

The MOSFETs all have an internal diode, therefore the transistor would turn on during every other cycle of the RF, shorting out the secondary coil half the time when it is forward biased. For this reason we implement a reverse biased diode for each secondary.

The tank circuit's primary function is the resonant circuit. Its main components are the secondary winding of the transformer and the trap "capacitor." We refer to it as the tank circuit since the LC circuit stores energy. Two lowpass filters are implemented, one for each secondary, to couple the DC input to the RF electrode pins [19]. A capacitor separates the tank circuit for secondaries 1 and 2 to isolate the signals at DC and short them at AC.

Using Eagle CAD, the schematic of the circuit first was separated by the two secondaries. Then it is broken down into the trapping functionality portion and the extracting functionality portion. Furthermore, the trapping portion consists of the tank circuit while the extracting portion consists of the quench and EV circuits. Figure 3.5 shows the circuit design in its entirety². Parts are in red and connections are in green. Only crossings where a dot is present indicate junctions. The schematic here is organized, from top to bottom as: tank circuit of electrode 1, tank circuit of electrode 2, quench circuit of secondary 1, quench circuit of secondary 2, extraction voltage circuit of secondary 1, and extraction voltage circuit of secondary 2.

The schematic was then coupled to the circuit board design layout using Eagle's features. The circuit is laid out such that the transformer and the tank circuit, or the path for the RF to the electrodes, runs centrally. On either side lie duplicate circuits, one for each secondary winding to allow for the high voltage offset for extraction (see

²Some errors are present in this figure. The DC/DC converter on the HV side of the EV circuit of secondary 1 (DC REG 6) should connect to both the pins of the voltage input (X10). A jumper wire was later used to fix this issue by using the DC/DC converter on the quench of secondary 1 (DCREG1) to power both portions of the circuit. The capacitors to ground on the driver chips of the quench and HV extraction circuits caused some complications, so they were made to float by connecting them to the extraction bias voltage.

Section 3.1). The board design in Eagle can be found in Fig. 3.6.

The circuit board design was then sent to a manufacturer. The layers of the

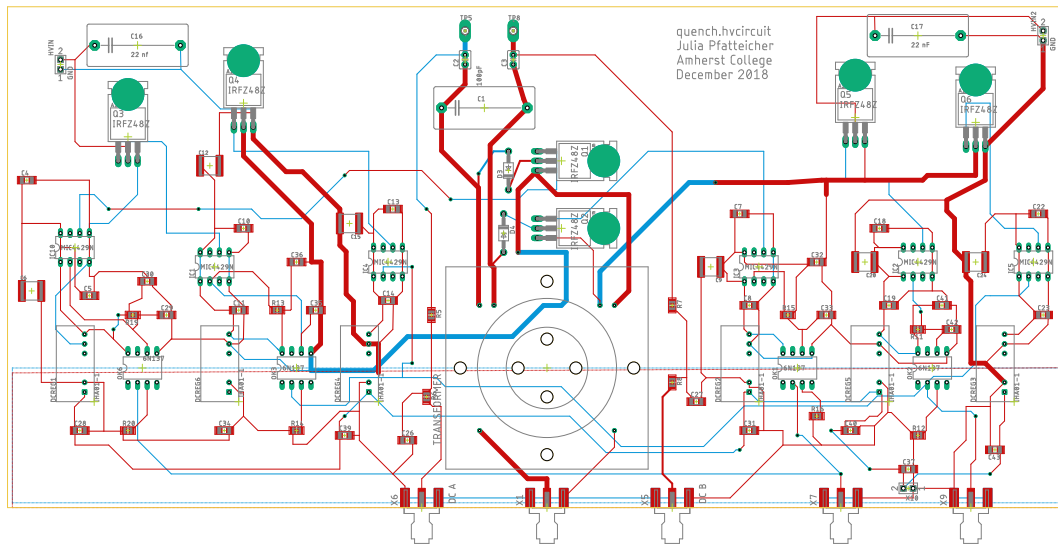


Figure 3.6: The circuit board design layout in Eagle. The dotted lines on the lower half of the board indicate the ground pour. The board is 27.8 cm by 13.3 cm.

board consist of a fiberglass core, a copper surface, and the silkscreen print on top to denote components and values. These layers are on either side of the fiberglass core, so parts can be attached and connections can be made on either side of the board. In the Eagle board file, red traces indicate a top trace and blue traces indicate a bottom trace. Vias connect through all layers to allow traces on either side of the board to merge. We implement a ground pour layer on the circuit to provide a ground plane for noise immunity. We omit this ground pour on any part of the circuit board where high voltages may be present to avoid arcing. Fig. 3.7 shows the final printed circuit

board before it was connected to the ion trap.

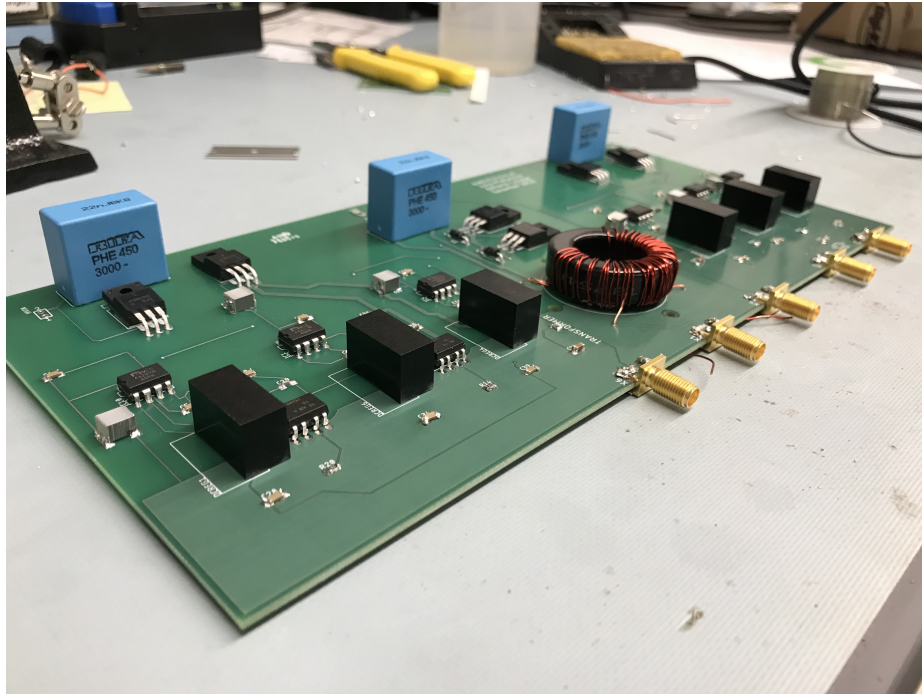


Figure 3.7: The circuit board itself prior to attachment to the trap. Note that not all traces are visible; some connect on the bottom of the circuit.

3.3 Circuit Design Considerations

The circuit's ideal functionality should, when probed, follow a radiofrequency signal which sharply rises to two slightly different high DC voltages. Naturally, all experiments come with complications and unexpected hurdles. As we strove for the ideal operation of the board, the following considerations were made.

One of the first visible issues was that on the left side of the board, the HV extraction voltage circuit's DC/DC converter was not being powered properly, as it was not properly connected to the voltage input. A jumper wire was used to connect the power input from the quench converter to also drive the driver chip of the HV extraction voltage circuit. With this wiring, a single DC/DC converter powered two

sections of the board instead of one.

This fix was sufficient in that it allowed the left side of the board to function, but the decrease in power caused an increase in the rise time as the signal rose to the HV. As a result, the two sides of the board were not functioning identically. The difference in wiring as well as the power difference caused the rise to HV to look markedly different, as seen in Fig. 3.8 and Fig. 3.9. The rise time for the left side of the board is approximately $3.75 \mu\text{s}$, as compared to the 600 ns rise time on the right side of the board.

For the rest of our observations, we focused on testing the right side of the board,

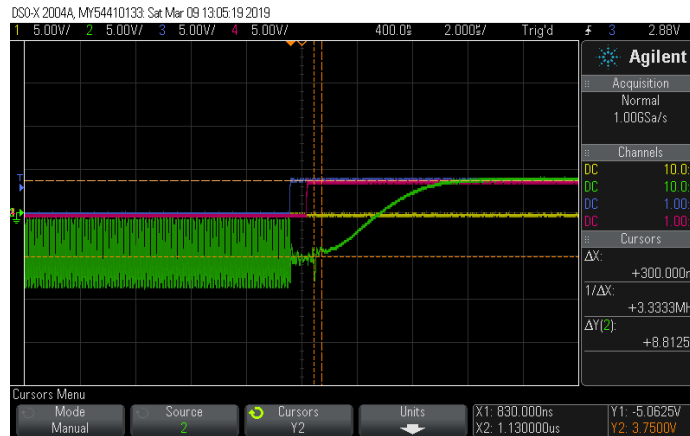


Figure 3.8: Scope image of the signal on the left side of the board (secondary 1). The timebase is $2 \mu\text{s}$ per division, and the voltage scale is 5 V per division. The blue channel indicates the quench trigger on the switch, the pink channel indicates the high voltage trigger on the switch, and the green channel indicates the voltage on the electrode connection pin. Rise time here is seen to be about $3.75 \mu\text{s}$.

since all traces were made properly from the start. We also considered that only one side of the board would be necessary for imminent experiments, as the TOFMS has yet to be attached to the ion trap. For now only the trapping functionality is immediately relevant, although proper operation of extraction was obviously still considered to confirm that the board could ultimately achieve its goal.

A characteristic that needed to be considered as well was the propagation time of

the optocoupler³, which is predicted to be between 250 and 400 ns. We see this delay when the extraction voltage circuit is being applied, as the high voltage trigger was occurring about 300 ns prior to actual rise to HV (see Fig. 3.9). The 300 ns delay is reproducible, so it can be accounted for in the application of the circuit by simply applying the HV trigger 300 ns prior to the time we want the extraction voltages to be applied to the electrodes.

Another time-based consideration that needed to be made was the rise time of the HV itself. We preferred a quick rise time, on the order of a few hundred nanoseconds [19], to maintain a good resolution of the ion cloud. This was achieved by inspecting capacitors C6, C12, C9, and C20 (the 1 μF film capacitors to ground on the driver chip, see Fig. 3.5). By allowing these capacitors to float rather than connect to real ground, the potential difference can remain at the 12 V from the DC/DC converter. Therefore the capacitor does not have to charge or discharge. We achieved this configuration by connecting these capacitors to the capacitors on the output of the driver chips (C4, C7, C10, and C18; see Fig. 3.5). By preventing them from having to charge up when the HV trigger was applied, the rise time was decreased from 30 μs to about 600 ns.

We also preferred a long dissipation time to allow for complete extraction of the ions out of the trap (on the order of tens of microseconds). To do so we inspected the AC coupling capacitors, C2 and C3, in the tank circuit. By using 10 μF capacitors instead of 0.1 μF capacitors, we lengthened the time constant from approximately 2 μs to 10 μs .

Another consideration that needed to be made was to ensure that the RF signal came through as a clean sine wave. The higher the peak-to-peak voltage, the more distorted the wave became. So when we decreased the RF voltage from 4.00 V_{pp} to 1.00 V_{pp} , the distortion of the wave decreased. Even more so we noticed that when

³Renesas PS9513, California Eastern Laboratories

we increased the frequency from what appeared to be resonance experimentally (6.4 MHz) closer to the theoretical resonance (9.3 MHz, set by the transformer), the distortion of the wave disappeared entirely. It is still unclear as to what was causing this relationship, but the transformer itself could be the reason that the wave quality improved when the frequency was increased based on its true resonance. Perhaps an RF switch with a higher voltage threshold should be used in the future, as its upper limit is 5 V (its frequency limit is plenty high enough that it need not be considered⁴). In any case, we were able to change the conditions appropriately so that when the board was attached to the trap it could operate properly.

A notable characteristic was the DC offset from zero we saw during testing (see Fig. 3.9). This offset occurs because the signal is spending half its time at the RF voltage and the other half at the extraction voltage. Therefore it is centering at its average voltage value, causing the offset. This characteristic was not present when the board was attached to the trap, since we were running at the RF most of the time and only pulsing the HV signal (see Fig. 3.12).

An important characteristic to consider was also the quality of the signal after the quench trigger was applied. A larger vertical spike was occurring just as the HV trigger was being applied, and it was preceded and followed by considerable ringing (see Fig. 3.9).

This idiosyncrasy was attributed to capacitive coupling between the gate and drain of the transistor. This quantity is referred to as the gate capacitance, gate-to-drain capacitance, or the reverse transfer capacitance. When the charge transfers to the channel, the gate makes a sudden step from one supply voltage to the other, transferring a “slug” of charge [25, Section 3.4]. This feature is called charge injection.

The transistor that was attached at this time was a power MOSFET (ON Semiconductors NDFP03N150CG). Its reverse transfer capacitance is 20 pF when the drain

⁴Mini Circuits, ZASWA-2-50DR+

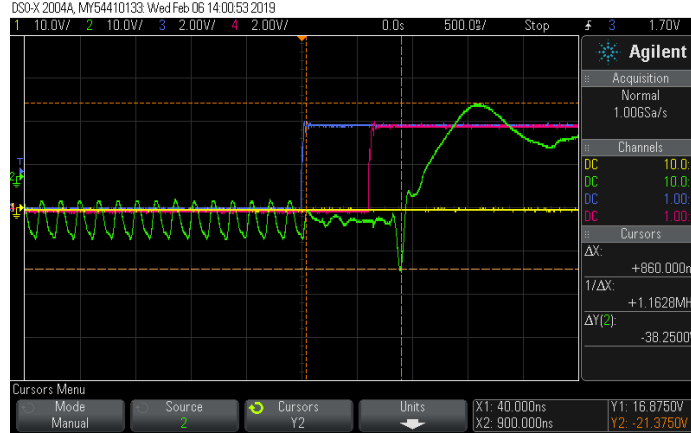


Figure 3.9: Scope image of the signal on the right side of the board (secondary 2). The timebase is 500 ns per division. The voltage scale for the green channel is 10 V per division, while the voltage scale is 2 V per division for the blue and pink channels. The blue channel indicates the quench trigger on the switch, the pink channel indicates the high voltage trigger on the switch, and the green channel indicates the voltage on the electrode connection pin. Rise time is approximately 600 ns, with a significant charge injection spike and overshoot to the high voltage. The incoming RF signal is distorted. Scope image taken using original MOSFET (NDFP03N150CG).

to source voltage is about 30 V. The lower the voltage, the higher the capacitance⁵, therefore the larger the charge injection that is carried over. Since we were testing at a low “high voltage,” typically 15 V, the gate-to-drain capacitance was likely closer to 100 pF. Replacing this transistor with a biMOSFET (IXYS IXBH16N170A) showed a considerable decrease in the charge injection spike, decreasing the spike height from about 11 V to 5 V (Fig. 3.11). This transistor has a typical reverse transfer capacitance of 31 pF when the collector to emitter voltage⁶ is 25 V. Although we do not know precisely the biMOSFET’s relationship between the collector-to-emitter voltage and the gate capacitance, it is likely similar. It appears as though the relationship may be less drastic, since the charge injection seemed to decrease with the same “high voltage” on the new transistor. These characteristics also seem to allude that if we run at a higher voltage input, the drain-to-source voltage (or collector-to-emitter

⁵<https://www.onsemi.com/pub/Collateral/ENA2232-D.PDF>

⁶The collector of a biMOSFET is comparable to the drain of a typical MOSFET, while the emitter is comparable to the source.

voltage) will also increase, creating an even smaller charge injection.

A biMOSFET is similar to a typical power MOSFET, but shares some characteristics with a bipolar junction transistor (BJT). A BJT operates via current control, while a MOSFET operates via voltage control. BJTs have three regions of silicon, allowing for both holes and electrons to carry charge. MOSFETs only allow for one type of charge carrier. An NPN type BJT uses primarily holes to carry charge, and a PNP type BJT uses primarily electrons. Meanwhile, MOSFETs only use one type of charge carrier (n-type or p-type) since it has only one region of silicon substrate [26]. A biMOSFET is still suitable for higher power applications like MOSFETs are, but uses both kinds of charge carriers. Fig. 3.10 shows the structure of a biMOSFET.

Although using a new transistor cleared up the signal and decreased the spike

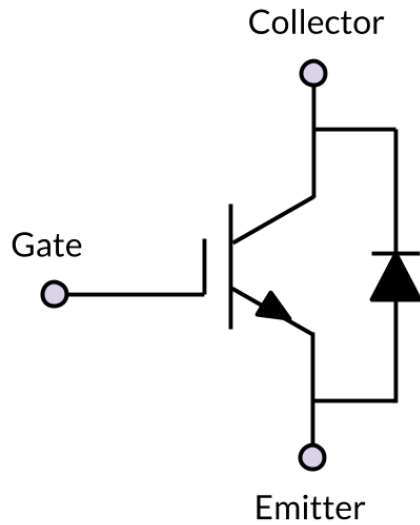


Figure 3.10: Diagram of a bipolar MOS transistor.

amplitude by more than half, the spike itself did not go away. A buffer capacitor of 22 nF sits between the HV input and the HV transistor, which acts as a local source of charge. Increasing the capacitance value to 10 μ F was attempted, but showed no improvement in the signal.

Another important characteristic to observe for a circuit like ours is the dissi-

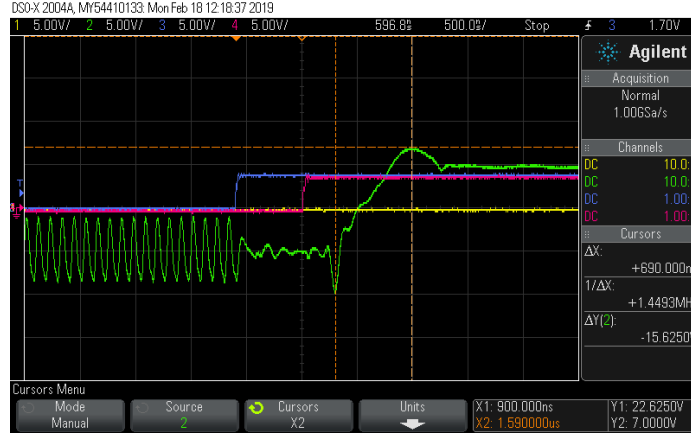


Figure 3.11: Scope image of the signal on the right side of the board (secondary 2) after attaching the biMOSFET (IXYS IXBH16N170A) from to the HV side of the extraction portion of the circuit. The timebase is 500 ns per division. The voltage scale for the green channel is 5 V per division for all channels. The blue channel indicates the quench trigger on the switch, the pink channel indicates the high voltage trigger on the switch, and the green channel indicates the voltage on the electrode connection pin. Charge injection spike is decreased and RF wave is cleaner. Scope image taken using biMOSFET.

pation time of the RF signal, which is set by the quench circuit. We are aiming to dissipate the RF within 1-2 RF cycles [19], which for 10 MHz is between 100 and 200 ns. Currently the dissipation time is about 100 ns, as seen in Fig. 3.11, where within about 1 cycle of the RF, the signal has dissipated to relative zero.

A characteristic that has yet to be fully understood is the overshooting when the signal rises to the high voltage. With a 15 V “high voltage” during testing, the signal rises up to 20 V and dissipates back down to 15 V within about 250 ns (see Fig. 3.12). This characteristic is even more interesting given that we do not see this occurrence on the left side of the board, where the power input to the circuits is decreased (see Fig. 3.8). Perhaps the power from the DC/DC converter in addition to the applied high voltage is causing some circuitry issues, causing the signal on the electrodes to overshoot before reaching the actual high voltage. More may be explored to fully comprehend this behavior.

After taking into consideration all the above concerns, we were able to achieve an

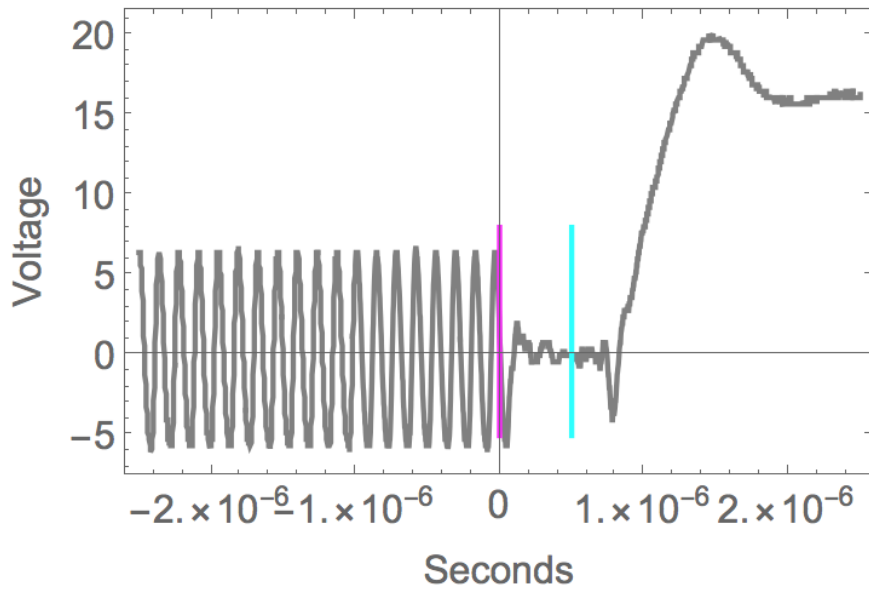


Figure 3.12: Ultimate implementation of the board resulted in the above graph of the voltage on the RF electrodes (gray trace), as the RF quenches rapidly (within 1 RF cycle, or 50 ns here) and the high extraction voltage is applied at the HV trigger. The magenta line indicates the quench trigger, and the cyan line indicates the HV trigger 500 ns later. Rise time on the HV is about 950 ns between the trigger and the peak. Charge injection spike has decreased further, to about 4 V amplitude. Graph depicts voltage on right side of the board, using the biMOSFET (IXYS IXBH16N170A).

improved signal quality that seemed promising for implementation on the ion trap. With a clear RF signal coming in and a minimized charge injection spike, as well as any delays accounted for, the board was ready to be attached to the trap. We moved onto attaching the RF pin of the trap to the electrode pinout on the right side of the board. Upon testing with the board finally attached, we were able to obtain even more precise data, as the capacitance of the resonator circuit was now the actual trap capacitance. This produced the signal seen in Fig. 3.12. We then were able to begin testing the board while applied to the ion trap and ensure proper operation.

Chapter 4

Implementation and Ion Clouds

In this chapter the application and usage of the board will be described as it pertains to the larger mission of the lab. The creation of ion clouds and the resulting ambitions we have for the board will be outlined.

4.1 Connecting the Board to the Trap

Once the board's design had been tested for proper operation, it could be attached to the ion trap itself for testing of functionality. We began with the motivation simply to trap the ions to see that replacing the former design's helical resonator [27] with the transformer was successful. This required only one side of the board to be in operation, since the RF electrodes are currently shorted together in the vacuum. The DC electrodes' voltages will need to be switched as well during the extraction phase, but in our current setup their voltage is controlled remotely. Their voltage is not a concern when considering the operation of the board in this phase.

With our previous setup, using the helical resonator instead of the transformer, we were able to locate the ions by adjusting the imager to search the trap as well as adjusting the lens of the UV beam that crystallizes the ions and allows them to fluoresce so they can be identified. Although these small imaging adjustments were

important, the laser frequency was most commonly to blame when we had trouble locating the ions. The UV beam cools the ions so that the ions' thermal energy is low enough that they cannot move around each other, allowing us to see them. Since the cooling linewidth of the resonance of beryllium is about 19.4 MHz in the UV, and the laser frequency is 319132.42 GHz, any very small change can affect our ability to actually crystallize the ions. Therefore it was important for us to regularly monitor the laser frequency to ensure that it did not mode-hop or deviate excessively from the precise frequency needed.

The DC electrodes, which trap the ions axially, are segmented into five smaller electrodes each. We ran the outer two electrodes at 10 V, the next inner electrodes at 2 V, and the innermost electrode at 0 V. These DC electrodes at such voltages create a nested well for the null where ions can reach stable equilibrium.

The transformer's resonant frequency is about one-fifth the resonant frequency of the helical resonator (7.3 MHz compared to 35 MHz), so we anticipated that the location of the crystal would be different for either apparatus. Namely, a higher resonant frequency corresponds to a tighter radial trap and therefore a narrower distribution of the crystal. Additionally, the deeper the axial well, the shallower the radial well. For this reason we presumed that the axial frequency would need to come down as well when applying the transformer. With the helical resonator, we began by gradually relaxing the axial frequency by decreasing the potential well depth, decreasing the voltage on electrodes 2 and 4. We noticed that as the axial trapping relaxed, the crystal shifted to the right on the imager (axially in the trap).

We then began to adjust the radial frequency by adjusting the power on the RF electrodes. We lowered it, to simulate the effects of the weaker trap formed by the board. As the RF power lowered, the ions shifted mostly in the vertical (on the imager and in the trap). With this information, and ions located, we moved onto attaching the board.

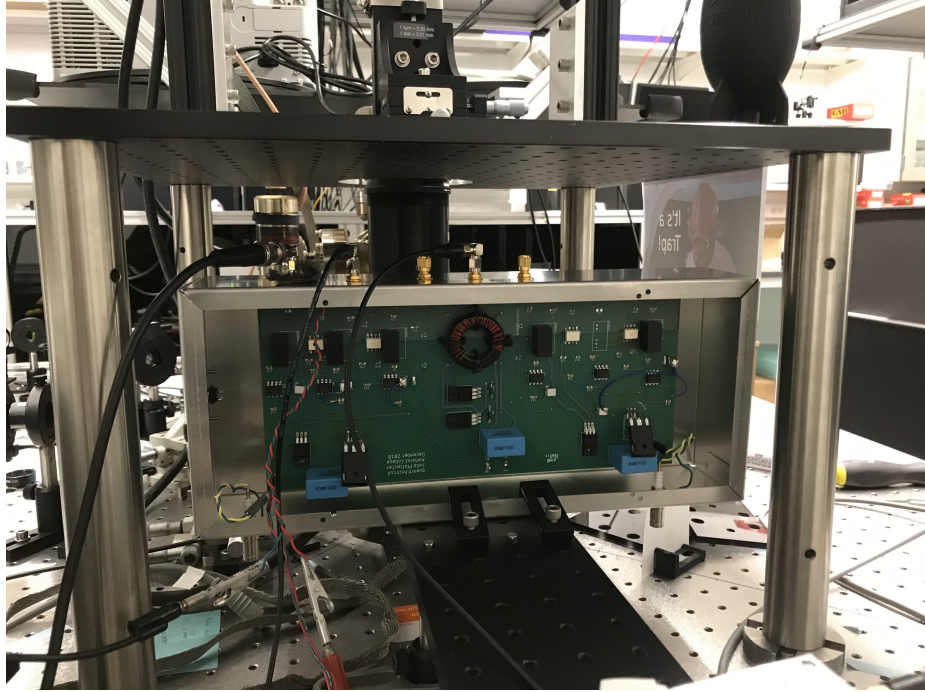


Figure 4.1: The circuit board in its enclosure, attached with feedthrough pin to the ion trap electrodes. The ion trap sits in a vacuum chamber behind the board.

In previous testing circumstances prior to attaching the transformer to the board, the resonant frequency of the transformer alone was 10.0 MHz with a step-up factor of 5.83 (with the scope probe acting as a 10 pF capacitor for the resonant circuit). When tested again after the transformer was attached to the board, with the same testing circumstances, its resonant frequency dropped to 9.3 MHz with a step-up factor of 2.85. This change in resonant frequency as well as the step-up factor is likely a result of the effects of the other parts on the board, as their impedances could affect the impedance matching, shifting the optimal voltage output to a different turn ratio.

The board was tested once again when it had been attached to the trap, with the board itself inside a metal enclosure for safety (see Fig. 4.1). The board was directly mounted to the trap with copper wires. In this configuration the resonance frequency was down to 7.3 MHz, with the same step-up factor of 2.85. In this case the

capacitance of the resonant circuit came from the trap capacitance, which is about 10 pF. The scope probe was set to 100X attenuation, forming a 5 pF capacitor. This small capacitance of the scope probe (5 pF) as well as any slight changes between our test capacitance and the trap capacitance are the probable causes of this change in resonant frequency. The scope probe’s capacitance is likely the biggest influencer. Since the capacitor of the probe and the trap “capacitor” are in parallel with one another, they form a total capacitance of 15 pF. Per Eq. 3.1, the resonant frequency of the transformer goes as the inverse of the square root of the capacitance. So, by changing the capacitance by a factor of 1.5, the frequency changes by a factor of about 0.8. Therefore a resonant frequency of 9.3 MHz would become about 7.4 MHz, which is what we observed.

Once the board was attached to the trap and testing ensured a smooth, RF output, the amplifier was connected. We ran the RF power up to 32 dBm, or 1.58 W. The RF signal produced had a voltage of 86 V_{pp}. This signal was measured on the RF feedthrough pin from the trap electrodes. At this power, the transformer did not get hot.

As our quest for ions began on the imager above the trap, we searched a wide range of values centered around where ions were found previously using the helical resonator with the weakened trap parameters. In this configuration the transformer alone was operating.

We tried setting the DC electrodes 2 and 4 to 0.5 V, to 2 V, and to 0.1 V, while running the RF power at 27 dBm, or 0.5 W. When the DC electrodes were at 0.5 V, the resonant frequency seemed to be up to 8 MHz. So, the q parameter was about 0.28, with a radial frequency of 870 kHz and an axial frequency of about 133 kHz. In that case the q parameter was the about same as it was with the helical resonator. When we changed the voltage on electrodes 2 and 4 to 0.1 V, the a parameter should be the same as it was with the helical resonator. In both cases with the axial and

radial trap relaxed, the crystal should simply be more spread out.

With the voltage at 0.1 V, the resonant frequency of the transformer seemed to be back at 7.3 MHz. We turned the RF power up to 32 dBm, and measured $84 V_{pp}$ on the RF feedthrough pin from the trap with the scope probe with 5 pF capacitance. Since we had only changed the radial frequency since attaching the board, we focused on making adjustments only the vertical. With small changes to the focus on the imager and the vertical position of the UV lens, we located the crystal of six ions (see Fig. 4.2).

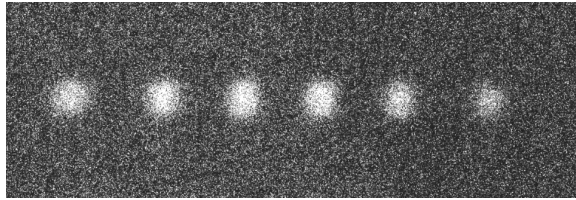


Figure 4.2: First Coulomb crystal found with the circuit board. Approximate distance between the first and second ions is $37 \mu\text{m}$.

4.2 Trapping Ions

With the ions trapped with the transformer, we began to look for more interesting characteristics of the updated trap and to find the boundaries and limitations of its usage. We began by squeezing the ions axially to see when the axial trapping would get tight enough that the radial trapping would be too weak to hold the ions. As we increased the voltage on the DC electrodes, we lost a few ions and some went dark. In addition, the location of the ions moved horizontally, as we expected. By the time we reached 10 V on electrodes 2 and 4, we had one by one lost all our ions. The ions that were present and then went dark (noted by the large space between two fluorescing ions) likely became beryllium hydride, as some background gas of hydrogen atoms could form a molecule with one of the beryllium ions (see Fig. 4.3).

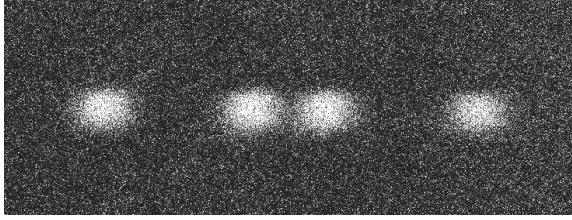


Figure 4.3: Coulomb Crystal of four beryllium ions and two dark ions, potentially beryllium hydride. Distance between innermost ions is $25 \mu\text{m}$, and between first and second ions is $51 \mu\text{m}$. DC electrodes 2 and 4 are at 0.4 V .

We reloaded the trap and started with a weaker axial trap, with electrodes 2 and 4 at 0.1 V . We stepped up the voltage on the DC electrodes and observed the ions' behavior again. We were able to tighten the trap up to 10 V on these electrodes again while still holding ions. When the voltage on those electrodes was about 6 V , we noticed that the ions began to form a diamond. This happens as the axial frequency approaches the radial frequency, so the ions do not see two separate degrees of freedom. Therefore they are free to move in both directions. We continued to step up the voltage and were still seeing a diamond-like shape with 9 V .

Because our trap geometry has the RF electrodes diagonal from one another, the radial alignment is tilted with respect to the focal plane of the imager. Therefore when the diamond shape forms, the ions begin to leave the 2D plane on which we observe them. In Fig. 4.4, we see that the ions in the middle are blurrier than those on the left and right. This is because of the diagonal alignment of the diamond, causing one ion to be below the focus of the imager and one to be above it. This is likely occurring just before the axial frequency matches the radial frequency. The middle ions are pushed off axis because the outside ions are strengthening the axial potential for the middle ions. We expect the ions to form a ring when the axial and radial frequencies are precisely the same, because then the ions will no longer crystallize. Some of the blurring on all ions is due to their micromotion.

With 10 V , the image was too blurry to distinguish exactly how many ions were

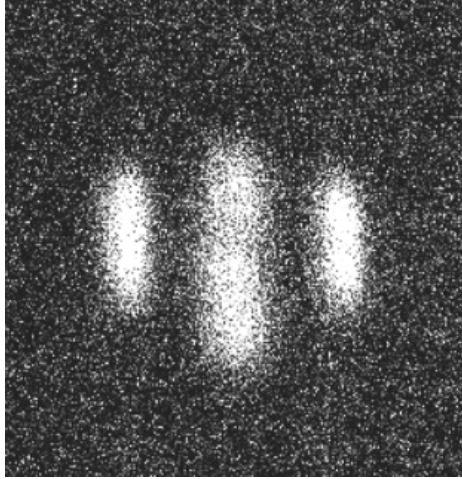


Figure 4.4: Coulomb crystal of four beryllium ions forming a diamond on the diagonal as the axial frequency approaches the radial frequency. The central ions are pushed off axis. Distance between leftmost and rightmost ions is $38 \mu\text{m}$. DC electrodes 2 and 4 are at 6 V.

present and how they were aligning, though they appeared to be forming a ring and decrystallizing (see Fig. 4.5). The blurring effect is due to the micromotion of the ions, as the frequency is high enough that the camera cannot capture individual ion positions.

Although the high visibility of the micromotion is interesting, we also hoped to observe the individual ions themselves. To do so, we put a differential voltage on the DC electrodes. This differential pushes the ions along the line between the two DC electrodes, which can bring them closer to the RF null, allowing for less micromotion and a clearer image.

With the voltage on the electrodes at 10 V, even with the differential, the ions were barely visible. As this axial frequency increases, the radial degree of freedom could become unstable as the a parameter shifts. Therefore it seems that either the trap is too weak here for them to crystallize, or that the axial frequency is high enough that they are moving around each other too quickly for us to see them.

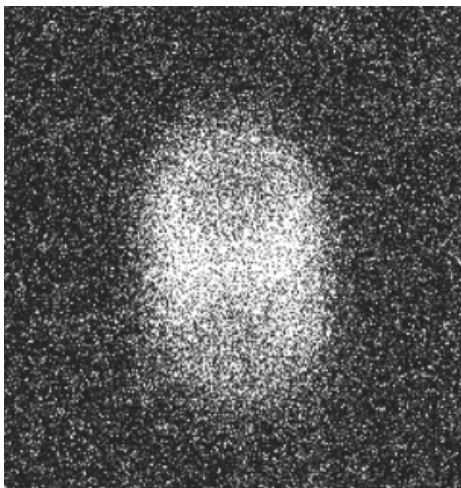


Figure 4.5: Ions in ring beginning to decrystallize. Horizontal diameter is $28.4 \mu\text{m}$. DC electrodes 2 and 4 are at 9 V.

4.3 Applying the Board to Test Switching

With ions successfully trapped and the trap configuration explored, we moved onto powering the rest of the board to applying the switch to high voltage. As we prepared to test the extraction stage (which would simply consist of loading the ions and switching to the high voltage to ensure that they leave the trap), a peculiar observation was made. We searched for the resonant frequency to see if it had moved once we had turned on the rest of the board, but we found that it was actually shifting depending on the power input. So, with 32 dBm input power, the resonant frequency was 8.7 MHz. At 36 dBm, it was 11.4 MHz. At 38 dBm, it was over 20 MHz. In fact, as we continued to explore this strange characteristic, we found that at 32 dBm, there was a second, even higher maximum about 20 MHz. It also was taking a significant amount more power input to achieve the same voltage output amplitude that we had before. We previously ran at $80 V_{pp}$, but now we seemed to only be able to reach 30-40 V_{pp} , regardless of frequency and power pairing. We previously found that we were able to trap and locate ions at a minimum voltage amplitude of $59 V_{pp}$, but under no circumstances were we able to achieve this voltage output anymore now

that the rest of the board was in operation.

Perplexed by this new hurdle, we began to look for places where something could be going wrong in our setup now that the rest of the board was in operation. Some ideas included the fact that a standing wave was forming between the transformer and amplifier, causing power to be reflected back, or that the amplifier itself was saturating. We attached a directional coupler to observe the reflected and forward signals. The reflected signal was consistently lower than the forward signal, though it did rise as power rose. We observed it to be between 60% and 83% reflected. Still, this is not enough to attribute all of our issue to the standing wave. Additionally, thermal energy loss can be ruled out as the signal amplitude is not rising steadily with power increase; it jumps suddenly at its resonance. The amplifier can be eliminated as a cause as well, because when we increase the input to the amplifier, we see a consistent increase in the amplifier's output going into the board. Meanwhile the board's output eventually decreases as the input increases. Therefore whatever is going wrong must be happening somewhere on the board itself.

These interesting characteristics are perplexing, and will require more time and research to achieve any conclusive answers. The transformer itself may require further investigation, or perhaps there is a wiring issue that was not apparent during testing. We may also wish to explore if new parameters will create a more effective environment for trapping ions. For now we are left with no other obvious areas to interrogate. Inconclusive results are never a scientist's goal, though they can leave us with interesting and thoughtful questions that are worth researching and exploring more.

Chapter 5

Concluding Thoughts

Although the board in its current state is capable of successfully trapping ions and rapidly quenching the RF signal, more work needs to be done to ensure that the extraction functionality will be successful. Furthermore, the apparatus of the TOFMS needs to be attached to the trap before we can achieve our future goal of measuring ions' time of flight. In this chapter the future ambitions of the board, as well as the overall project, will be discussed.

5.1 Small-Picture Goals

The ultimate goal for the board itself is to confirm that it is capable of trapping ions and expelling them to the TOFMS successfully. Although we have demonstrated each of these steps separately, and can switch between them, we have yet to demonstrate the success of the entire process in practice. With that in mind, one of the primary future plans with the board is to fix the issue of the spikes that are occurring as the signal switches from the RF to the HV signal. Although we have been able to drastically decrease the spike size, the characteristic has not been eradicated completely. This problem could potentially cause issues of extracting the ions cleanly and

uniformly and therefore affect the accuracy of the measurement on the mass spectrometer.

So far we have attributed the problem to the charge injection of the transistor due to capacitive coupling between the gate and the drain. We also know that a higher input voltage should create a higher drain-to-source voltage, creating a smaller reverse transfer capacitance and therefore a smaller charge injection. Although this information is valuable and has led to decreasing the charge injection spike by more than half, further testing is required to fully understand this relationship and achieve the minimum charge injection for successful expelling of the ions from the trap.

We currently are looking more into the other capacitances within the transistor that may be affecting the charge injection. Namely, the relationship between the output capacitance (C_{oss}) and the reverse transfer capacitance (C_{rss}) may be relevant (see Fig. 5.1). When testing the board with a new MOSFET that others with a similar board configuration used [19], the signal quality decreased drastically. Additionally, the HV rise time was lengthened. Although its reverse transfer capacitance is marginally higher, the value $C_{oss} - C_{rss}$ is significantly more than that of the other transistors. Based on our understanding so far, it is the difference between these two values that actually impacts the output signal. Additionally, we may want to explore the influence of the gate resistance of the MOSFETs, since these resistance values are generally high. A higher resistance would cause the gate capacitor to take more time to charge up, creating a longer time constant and/or a bigger charge injection. This seems plausible, since a biMOSFET does not share this quality of a high on-resistance with regular MOSFETs, and we observed a decreased charge injection with the biMOSFET. For these reasons we may wish to inspect the structure of the MOSFET further to fully understand the system and its behavior.

Additionally, the transistor in use on the HV portion of the circuit (the biMOSFET) has a voltage limit of 1700 V. Although this is sufficient in the short-term, we

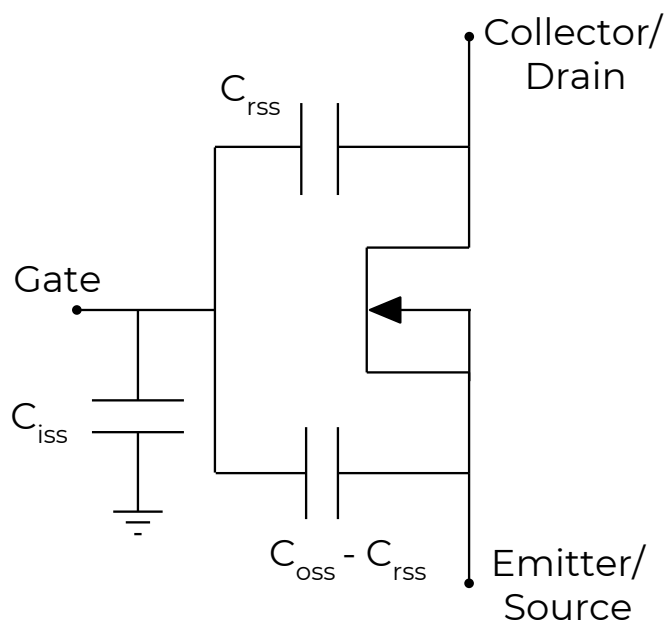


Figure 5.1: The structure of a MOSFET and its internal capacitances, as we currently understand them. C_{iss} indicates the input capacitance, C_{oss} indicates the output capacitance, and C_{rss} indicates the reverse transfer capacitance.

may want to increase the voltage in the future to allow for ample experimentation. Especially since we think that a higher voltage on the HV input could decrease our issues of charge injection, it may be useful to implement a different transistor with a higher voltage allowance later. Furthermore, if a new, updated board is produced, allowing for a larger footprint, a larger transistor can be properly implemented.

A feature that has yet to be fully understood is the ringing that occurs between the quench trigger and the high voltage trigger. It does not appear to be related to the charge injection, since the charge injection should be a single spike. Additionally, the ringing did not appear to change drastically with the new transistor, while the charge injection spike did. Namely, the amplitude remained around 2 V and the

number of oscillations did not change. We also can rule out noise or pickup from the room, as the ringing is reproducible. Perhaps more needs to be investigated about the transformer, as ringing can be result a signal reflection due to improper impedance matching [28].

With the types of experiments we are working on now, only one side of the board is needed since we are not yet ready to apply high extraction voltages. Once we are ready to extract to ions to the TOFMS, both sides of the board will need to be in use to apply the two different high voltages to the electrodes. Since in its current state, only one side works reliably and well, the other side will need to be improved before extraction will be possible. Namely, the rise time on the left side of the board would ideally be shorter, as it is $3.75 \mu\text{s}$ now, while the right side rise time is 600 ns. Having the time scale on the order of a hundreds of nanoseconds is ideal, as others on this time scale have successfully measured ion time of arrival on a TOFMS [19]. In addition, it is preferable to have the signals on both sides of the board to be identical, which they are not currently. A reproduction of the board with traces issues fixed should solve this problem.

We also currently control the DC electrodes using a software system to set each electrode voltage remotely. Although this is useful in the trapping stage, more needs to be done so that we can switch the DC electrodes to high extraction voltages at the same time as the RF electrodes. The program we use now does not operate on a short enough timescale for us to do this, nor does it possess the ability to switch to a high enough voltage. We may choose to implement another, simpler version of the board we have now for the RF electrodes. This will consist of a similar transistor switching configuration without some of the quench and tank circuit components that are necessary to switch from an AC to DC signal. Further work will need to be done to account for any delay times present in that circuit due to optocouplers or other components. With that in mind we may set all the electrodes to switch to the

extraction voltages at precisely the same time, ensuring that the ion cloud is expelled cleanly from the trap.

5.2 Big-Picture Goals

An important next step in our lab is to attach the TOF arm to the ion trap, and to trap O_2^+ molecular ions with the beryllium atomic ions we can trap currently. Presently we can photoionize oxygen and can observe the photoionization spectrum with the TOFMS. This apparatus, which consists of the valve, pump, skimmer, and ionization beam, needs to be attached to the trap in its entirety. Once the apparatus setup is complete, we will be able to drive the two-photon transitions between vibrational states. With REMPI, we can ionize the oxygen molecules. We may then form a Coulomb Crystal consisting of beryllium atomic ions and oxygen molecular ions by using the RF signal from the transformer to create a stable equilibrium inside the trap, as discussed previously. Through state-selective dissociation, the crystal formation should shift as molecular ions are dissociated. The circuit board then can rapidly quench the RF signal on the RF electrodes, and apply the high extraction voltages to the RF electrodes. The other circuit board will also apply the high extraction voltages to the DC electrodes. With these high voltages applied, the ions will expel out of the trap and into the TOFMS. They will be accelerated forward towards the 0 V plate, and then enter the lens to maintain their trajectory. They will focus on the MCP for detection and mass analysis. Through mass analysis on the TOFMS, we may determine if the transition was driven successfully.

By monitoring the transition frequency over long times with this setup, we may interpret the stability of the transition and therefore learn more about the proton-to-electron mass ratio variation. If we are to observe that the frequency changes through time, and therefore so does μ , then we will have discovered new phenomena relevant

to the Standard Model [3]. We hope to contribute to the endeavor of understanding elusive and fascinating fundamental constants, as we actively lean into the ambiguity and uncertainty new physics brings.

Bibliography

- [1] J. Mitchell, “A Case of You,” **Blue** (1970), URL <http://jonimitchell.com/music/song.cfm?id=181>.
- [2] R. Carollo, A. Frenett, and D. Hanneke, “Two-Photon Vibrational Transitions in $^{16}\text{O}_2^+$ as Probes of Variation of the Proton-to-Electron Mass Ratio,” *Atoms* **7**, 1 (2018).
- [3] A. Frenett, *State-selective Production of Oxygen Molecular Ions for New Physics Searches*, Undergraduate thesis, Amherst College (2018).
- [4] T. Zelevinsky, S. Kotochigova, and J. Ye, “Precision Test of Mass-Ratio Variations with Lattice-Confined Ultracold Molecules,” *Phys. Rev. Lett.* **100**, 043201 (2008).
- [5] M. Kajita, G. Gopakumar, M. Abe, M. Hada, and M. Keller, “Test of m_p/m_e changes using vibrational transitions in N_2^+ ,” *Phys. Rev. A* **89**, 032509 (2014).
- [6] L. Hilico, N. Billy, B. Grémaud, and D. Delande, “Polarizabilities, light shifts and two-photon transition probabilities between $J = 0$ states of the H_2^+ and D_2^+ molecular ions,” *J. Phys. B* **34**, 491 (2001).
- [7] J.-P. Karr, “ H_2^+ and HD^+ : Candidates for a molecular clock,” *J. Mol. Spec.* **300**, 37 (2014), ISSN 0022-2852.

- [8] P. F. Sta anum, K. Høj bjerre, P. S. Skyt, A. K. Hansen, and M. Drewsen, “Rotational laser cooling of vibrationally and translationally cold molecular ions,” *Nature Phys.* **6**, 271 (2010).
- [9] A. Sur, C. V. Ramana, and S. D. Colson, “Optical spectra of the lowest Π_g Rydberg states in O_2 ,” *J. Chem. Phys.* **83**, 904 (1985).
- [10] H. Park, P. J. Miller, W. A. Chupka, and S. D. Colson, “Production of vibrationally state-selected O_2^+ via newly discovered $4s-3d$ and $5s-4d$ Rydberg states of O_2 ,” *J. Chem. Phys.* **89**, 3919 (1988).
- [11] R. Ogorzalek Loo, W. J. Marinelli, P. L. Houston, S. Arepalli, J. R. Wiesenfeld, and R. W. Field, “Multiphoton ionization of O_2 $X^3\Sigma_g^-$, $a^1\Delta_g$, and $b^1\Sigma_g^+$ via the two-photon resonant $ns\sigma_g$, $nd\sigma_g$, and $nd\pi_g$ Rydberg levels,” *J. Chem. Phys.* **91**, 5185 (1989).
- [12] A. Sur, R. S. Friedman, and P. J. Miller, “Rotational dependence of the Rydberg-valence interactions in the $^1\Pi_g$ states of molecular oxygen,” *J. Chem. Phys.* **94**, 1705 (1991).
- [13] A. Dochain and X. Urbain, “Production of a rovibrationally selected O_2^+ beam for dissociative recombination studies,” *EPJ Web of Conferences* **84**, 05001 (2015).
- [14] W. Paul, “Electromagnetic traps for charged and neutral particles,” *Rev. Mod. Phys.* **62**, 531 (1990).
- [15] A. W. S. Tong, X.; Winney, “Sympathetic Cooling of Molecular Ions in Selected Rotational 545 and Vibrational States Produced by Threshold Photoionization,” *Phys. Rev. Lett.* **105**, 143001 (2010).
- [16] M. Germann, X. Tong, and S. Willitsch, “Observation of electric-dipole-forbidden infrared transitions in cold molecular ions,” *Nature Phys.* **10**, 820 (2014).

- [17] T. Schneider, B. Roth, H. Duncker, I. Ernsting, and S. Schiller, “All-optical preparation of molecular ions in the rovibrational ground state,” *Nature Phys.* **6**, 275 (2010).
- [18] C.-Y. Lien, C. M. Seck, Y.-W. Lin, J. H. Nguyen, D. A. Tabor, and B. C. Odom, “Broadband optical cooling of molecular rotors from room temperature to the ground state,” *Nature Comm.* **5**, 4783 (2014).
- [19] P. C. Schmid, J. Greenberg, M. I. Miller, K. Loeffler, and H. J. Lewandowski, “An ion trap time-of-flight mass spectrometer with high mass resolution for cold trapped ion experiments,” *Rev. Mod. Phys.* **88**, 123107 (2017).
- [20] P. K. Ghosh, *Ion Traps* (Oxford University Press, 1996).
- [21] D. Leibfried, R. Blatt, C. Monroe, and D. Wineland, “Quantum dynamics of single trapped ions,” *Rev. Mod. Phys.* **75**, 281 (2003).
- [22] D. Yerchuck, A. Dovlatova, Y. Yerchak, and F. Borovik, “Analytical Solution of the Mathieu Equation,” (2014).
- [23] S. Qiao, *Constructing a Linear Paul Trap System for Measuring Time-variation of the Electron-Proton Mass Ratio*, Undergraduate thesis, Amherst College (2013).
- [24] *The ARRL Handbook for Radio Communication* (ARRL, Newington, Connecticut, 2008), ISBN 0-87259-101-8.
- [25] P. Horowitz and W. Hill, *The Art of Electronics* (Cambridge University Press, New York, NY, USA, 1989), ISBN 0-521-37095-7.
- [26] Ian, “Difference Between BJT and MOSFET,” (2018),
 URL <http://www.differencebetween.net/technology/difference-between-bjt-and-mosfet/>.

- [27] P. A. Kyaw, *Constructing an Ultra-High Vacuum Chamber and a Radio Frequency Helical Resonator for Trapping Ions*, Undergraduate thesis, Amherst College (2014).
- [28] J. Heath, “Reducing ringing or reflections by controlling impedance lines,” (2018), URL <https://www.analogictips.com/reducing-ringing-or-reflections-by-controlling-impedance-lines-faq/>.